Science AAAS

www.sciencemag.org/cgi/content/full/science.1256758/DC1

Supplementary Materials for

Thermal structure of an exoplanet atmosphere from phase-resolved emission spectroscopy

Kevin B. Stevenson,* Jean-Michel Désert, Michael R. Line, Jacob L. Bean, Jonathan J. Fortney, Adam P. Showman, Tiffany Kataria, Laura Kreidberg, Peter R. McCullough, Gregory W. Henry, David Charbonneau, Adam Burrows, Sara Seager, Nikku Madhusudhan, Michael H. Williamson, Derek Homeier

*Corresponding author. E-mail: kbs@uchicago.edu

Published 9 October 2014 on *Science* Express
DOI: 10.1126/science.1256758

This PDF file includes:

Materials and Methods
Supplementary Text
Figs. S1 to S8
Tables S1 and S2
Caption for movie S1
References

Other Supplementary Material for this manuscript includes the following:
(available at www.sciencemag.org/cgi/content/full/science.1256758/DC1)

Movie S1

Materials and Methods

Each phase curve visit consists of 13 or 14 *HST* orbits and each primary transit or secondary eclipse visit consists of four orbits. To improve observational efficiency, the telescope operated in spatial scan mode, scanning at a rate of $0.08''\mathrm{s}^{-1}$ and alternating between the forward and reverse directions. In each scan direction, the instrument made 15 non-destructive reads (SPARS10 sampling) over 103 seconds, the maximum duration possible with these settings. The observations achieved a duty cycle of $\sim$73%. Typically, we acquired 19 exposures per *HST* orbit and 1151 exposures total over all visits. In the extracted 1D spectra, we achieved a signal-to-noise ratio (S/N) of $\sim$1,300 per pixel. This corresponds to a S/N of $\sim$3,300 per spectrophotometric bin of width 7 pixels.

The WFC3 spatial scan data contain a previously-documented orbit-long systematic that we fit with an exponential ramp model component. The ramp systematic is steepest during the first *HST* orbit and nearly consistent in shape over the remaining orbits. Some visits have second *HST*-orbit ramps that are also noticeably steeper. Accordingly, we do not include data from the first orbit and, when necessary, fit an additional exponential ramp model component to the second orbit. Excluding the second orbit from the phase-curve data does not change our conclusions.

To model each visit-long trend, we use a linear function for the five shorter eclipse/transit observations and a quadratic function for the three longer phase-curve observations. In each case, we use the Bayesian Information Criterion (BIC) to determine the appropriate order of polynomial. Using a quadratic trend for the transit/eclipse observations does not change our results. Using a linear trend for the phase-curve observations results in poor fits in which phase-curve minima fall below the in-eclipse flux (which is physically impossible) for many of the channels. We also tested multi-visit-long sinusoid models with various periods, but could not achieve better fits than those presented in our final analysis. We include the curved flux baseline (from the planet's phase variation) in the transit and eclipse models so as to not bias the measured depths.

The sinusoidal function used to represent the band-integrated (white light) phase variation takes the form $c_1 \cos[2\pi(t-c_2)/P] + c_3 \cos[4\pi(t-c_4)/P]$, where t is time, P is the planet's orbital period, and c_1 - c_4 are free parameters. The second sinusoidal term allows us to fit for an asymmetric phase curve, which we detect with $\sim 10\sigma$ confidence in the white light curve data. We do not detect changes in the light-curve due to ellipsoidal variation in the shape of the planet or host star.

In the spectroscopic phase curves, we do not detect statistically significant asymmetry; therefore, we fix c_3 and c_4 to zero. Additionally, we fix the ratio between the semi-major axis and the stellar radius ($a/R_\star$) and the cosine of the inclination ($\cos i$) in the spectroscopic fits using best-fit values from the white light curve data. Each spectrophotometric channel shares a common set of eclipse-depth and phase-curve parameters.

We estimate uncertainties using a differential-evolution Markov-chain Monte Carlo (DE-MCMC) algorithm. Assuming the flux variation is solely from the planet, it is unphysical for the phase-curve to fall below the in-eclipse flux, so we apply an asymmetric prior to c_1 (the phase-curve amplitude) wherein credible amplitudes have an uninformative prior and unphysical amplitudes have a Gaussian prior with a standard deviation equal to the eclipse depth uncertainty in each spectrophotometric channel.

In our analyses of the spectroscopic data, we tested both sinusoid and double-sinusoid models when fitting the phase curves. We find that the double sinusoid is unjustified according to the BIC. Nonetheless, we explored the dependence of our free parameters on our choice of model. Both sets of eclipse depths are consistent to well-within 1σ. We also find that the phase-curve amplitudes in 13 of the 15 channels are consistent at the 1σ level, and all channels are consistent to within 2σ. Although the computed uncertainties in the phase-curve amplitudes and peak offsets for both model combinations are also consistent, we note that four channels exhibit some model dependence ($> 2\sigma$) in their best-fit peak offsets. Relative to the pressure-peak offset trend observed in Fig. S7, some outliers with the sinusoid model achieve more consistent peak offsets with the double sinusoid. However, the latter is also true as some consistent peak offsets with the sinusoid model become outliers with the double sinusoid. Ultimately, one model combination does not consistently achieve more reliable results than the other.

Supplementary Text

Observations of the thermal emission from the dayside and night side of a planet can inform us on its Bond albedo and heat redistribution efficiency. Here we derive, using energy balance, the Bond albedo and our metric for estimating the redistribution efficiency. We need not make use of any reflected-light observations. First, we must derive the bolometric dayside and night-side fluxes (and their uncertainties) by integrating over wavelength an ensemble of spectra from the MCMC retrieval. The model spectra are only constrained over the WFC3 bandpass; however, a majority of the flux emanates from near- to mid-infrared wavelengths. Therefore, we use the MCMC ensemble of fitted atmospheric properties to predict the planetary spectrum out to 20 μm. This extrapolation contributes to most of the uncertainty in the measured bolometric fluxes. Upon integrating, we obtain a dayside bolometric flux, F_{day}, of $(3.9 - 4.1) \times 10^5$ W m^{-2} and a night-side bolometric flux, F_{night}, of $(0.00024 - 0.18) \times 10^5$ W m^{-2} . With these bolometric fluxes, we can compute the desired quantities.

First, we derive the Bond albedo. Assuming all of the energy absorbed by the planet is re-radiated and neglecting internal heat from within the planet, we obtain the following relation:

$$S_\star(1 - A_{\mathrm{B}})\pi R_{\mathrm{p}}^2 = 2\pi R_{\mathrm{p}}^2(F_{\mathrm{day}} + F_{\mathrm{night}}), \tag{1}$$

where $A_{\rm B}$ is the Bond albedo and $R_{\rm p}$ is the planet radius. The stellar flux at the planet, $S_\star$, is given by:

$$S_\star = \sigma T_\star^4 \left(\frac{R_\star}{a}\right)^2, \tag{2}$$

where σ is the Steffan-Boltzman constant, $T_\star$ is the stellar effective temperature, $R_\star$ is the stellar radius, and a is the planet's semi major axis. The left-hand-side (LHS) of Equation 1 is the stellar flux incident upon the planet and the right-hand-side (RHS) is the flux re-radiated from the planet. Using our computed $F_{\rm day}$ and $F_{\rm night}$ values, the measured stellar effective temperature (4520 $\pm$120 K), and the measured $a/R_\star$ (4.855 $\pm$ 0.002), we determine the Bond albedo to be 0.078 – 0.262.

Second, we rewrite the heat redistribution efficiency in terms of our observed quantities. If both planet sides have the same temperature ($F_{\rm day}$= $F_{\rm night}$, full redistribution) then Equation 1 becomes:

$$S_\star(1 - A_{\rm B})\pi R_{\rm p}^2 = 4\pi R_{\rm p}^2 F_{\rm day}\mathcal{F}, \tag{3}$$

where $\mathcal{F}$ is the redistribution factor, which is unity in the case of full redistribution. We equate the RHS of Equation 1 to the RHS of Equation 3 and then solve for the redistribution factor:

$$\mathcal{F} = \frac{1}{2}(1 + \frac{F_{night}}{F_{day}}). \tag{4}$$

In the case of full redistribution ($F_{\rm day}$= $F_{\rm night}$), we recover $\mathcal{F} = 1$. If there is no redistribution, meaning all of the flux emanates from only the dayside ($F_{\rm night}$= 0), then $\mathcal{F} = 0.5$. Inputing the measured $F_{\rm day}$ and $F_{\rm night}$ values, we find that $\mathcal{F}$ = 0.500 – 0.524.

Table S 1: **Best-Fit White Light Parameters with 1σ Uncertainties**

Parameter	Value
Transit Times (BJD_{TDB})	2456601.02729(2)
	2456602.65444(2)
	2456603.46792(2)
	2456605.90822(2)
	2456612.41604(3)
	2456615.66978(1)
$R_p/R_\star$	0.15948(4)
$a/R_\star$	4.855(2)
$\cos i$	0.13727(19)
Eclipse Times (BJD_{TDB})	2456601.43503(16)
	2456602.25412(14)
	2456603.87485(13)
	2456608.75729(23)
	2456632.34584(12)
Eclipse Depth (ppm)	461(5)
c_1 (ppm)	234(2)
c_2 (BJD_{TDB})	2456601.4290(12)
c_3 (ppm)	29(1)
c_4 (BJD_{TDB})	2456601.3486(15)

BJD_{TDB}, Barycentric Julian Date, Barycentric Dynamical Time; ppm, parts per million. Parentheses indicated 1σ uncertainties in the least significant digit(s).

Table S 2: **Best-Fit Spectroscopic Parameters with 1σ Uncertainties**

Wavelength (μm)	PC amplitude (ppm)	PC peak offset (minutes)	Eclipse depth (ppm)	Dayside T_B (K)
1.1425	177±16	-28±32	367±45	1,766±31
1.1775	213±13	-28±24	431±39	1,782±23
1.2125	215±13	-57±24	414±38	1,748±24
1.2475	242±12	-51±20	482±36	1,770±20
1.2825	216±15	12±18	460±37	1,736±22
1.3175	212±17	-26±21	473±33	1,724±19
1.3525	186±10	63±26	353±34	1,628±24
1.3875	167±10	-51±26	313±30	1,581±24
1.4225	162±11	-11±21	320±36	1,567±28
1.4575	206± 7	23±13	394±36	1,605±24
1.4925	228± 9	-6±17	439±33	1,615±21
1.5275	244± 5	-3±17	458±35	1,624±21
1.5625	306± 8	-8±11	595±36	1,687±19
1.5975	309±12	-9±12	614±37	1,684±19
1.6325	344±17	-12±12	732±42	1,732±19

PC, phase curve; ppm, parts per million. The peak offset is with respect to the fixed time of mid-eclipse, as determined from a white-light-curve fit. We use a stellar Kurucz model when estimating the dayside brightness temperatures (T_B).

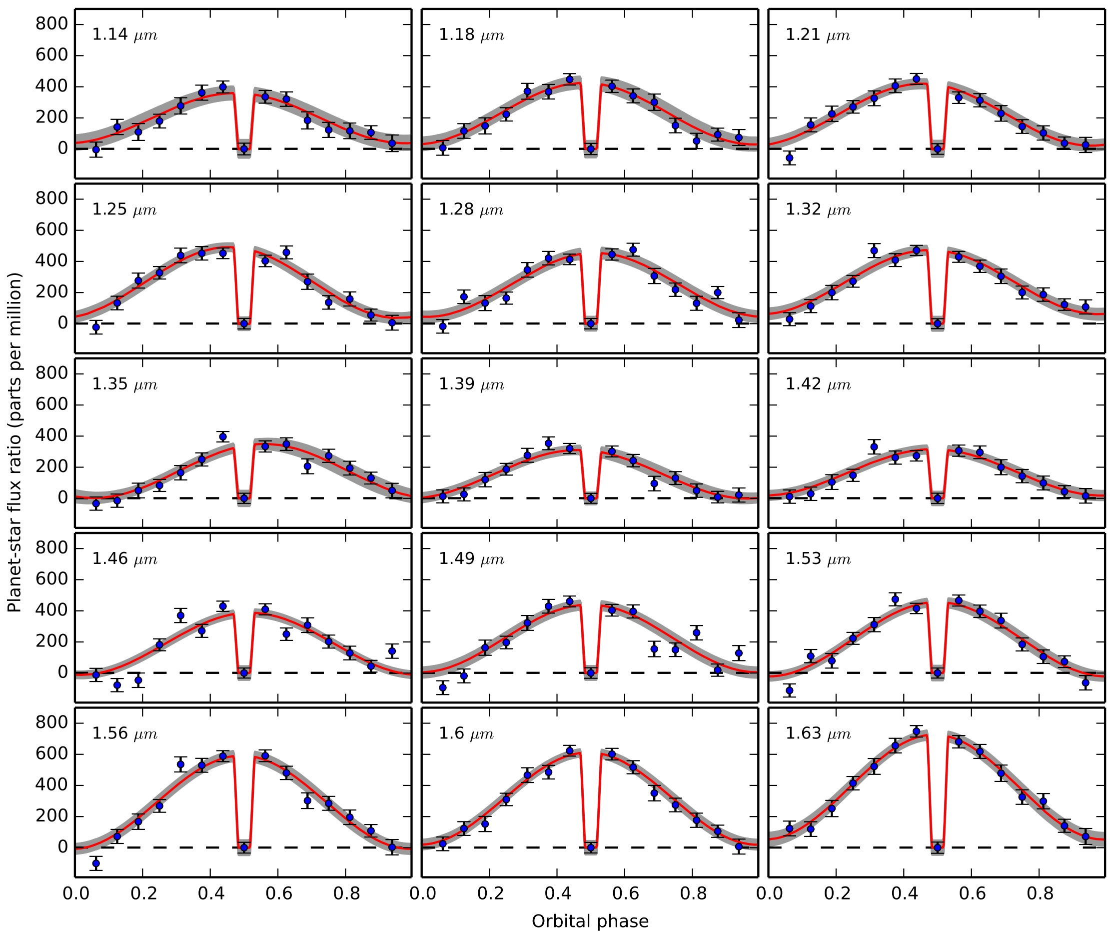

Fig. S 1: **Spectroscopic phase curves of WASP-43b.** Red curves indicate median models to the blue data points with 1σ uncertainties. The gray regions indicate model 1σ uncertainty regions.

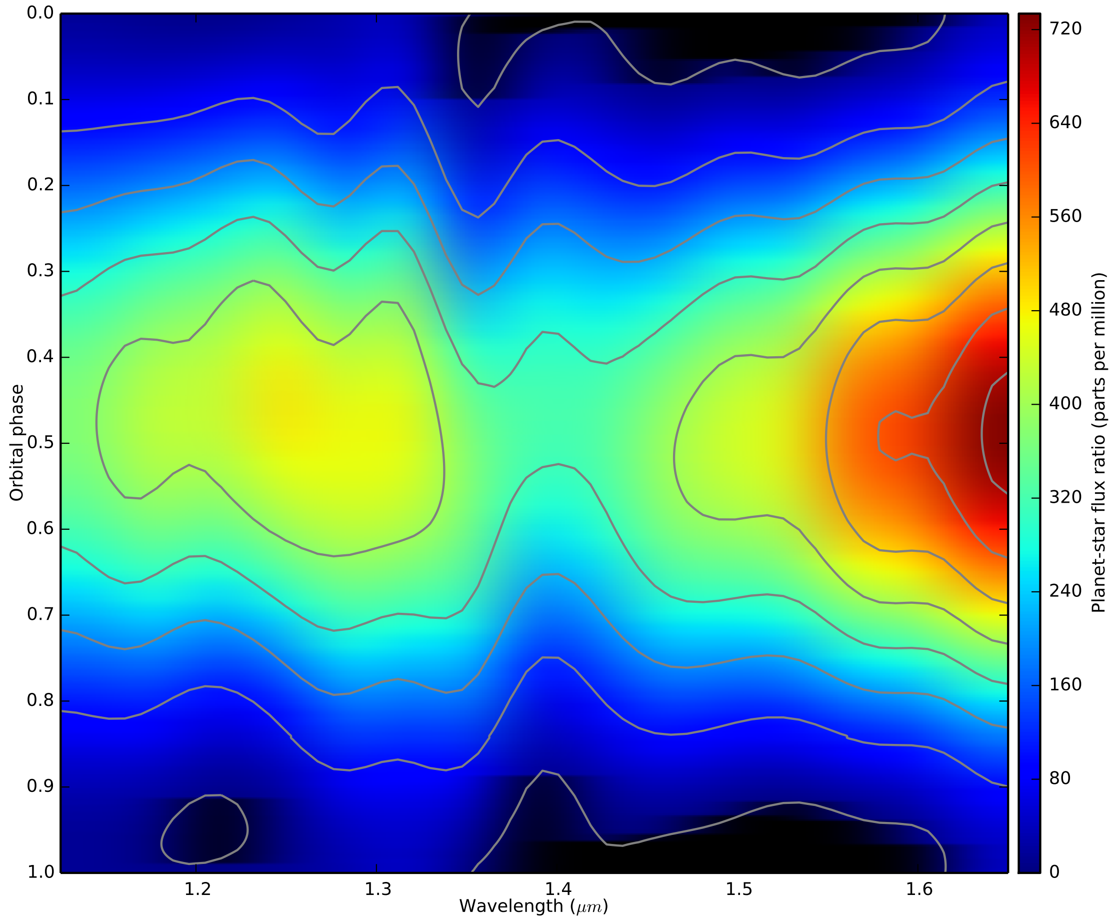

Fig. S 2: **Phase-resolved emission spectrum of WASP-43b relative to the stellar flux.** To generate this map, we apply bi-cubic interpolation between our 15 best-fit spectroscopic phase curve models. The eight contour lines are evenly spaced from minimum to maximum planet emission.

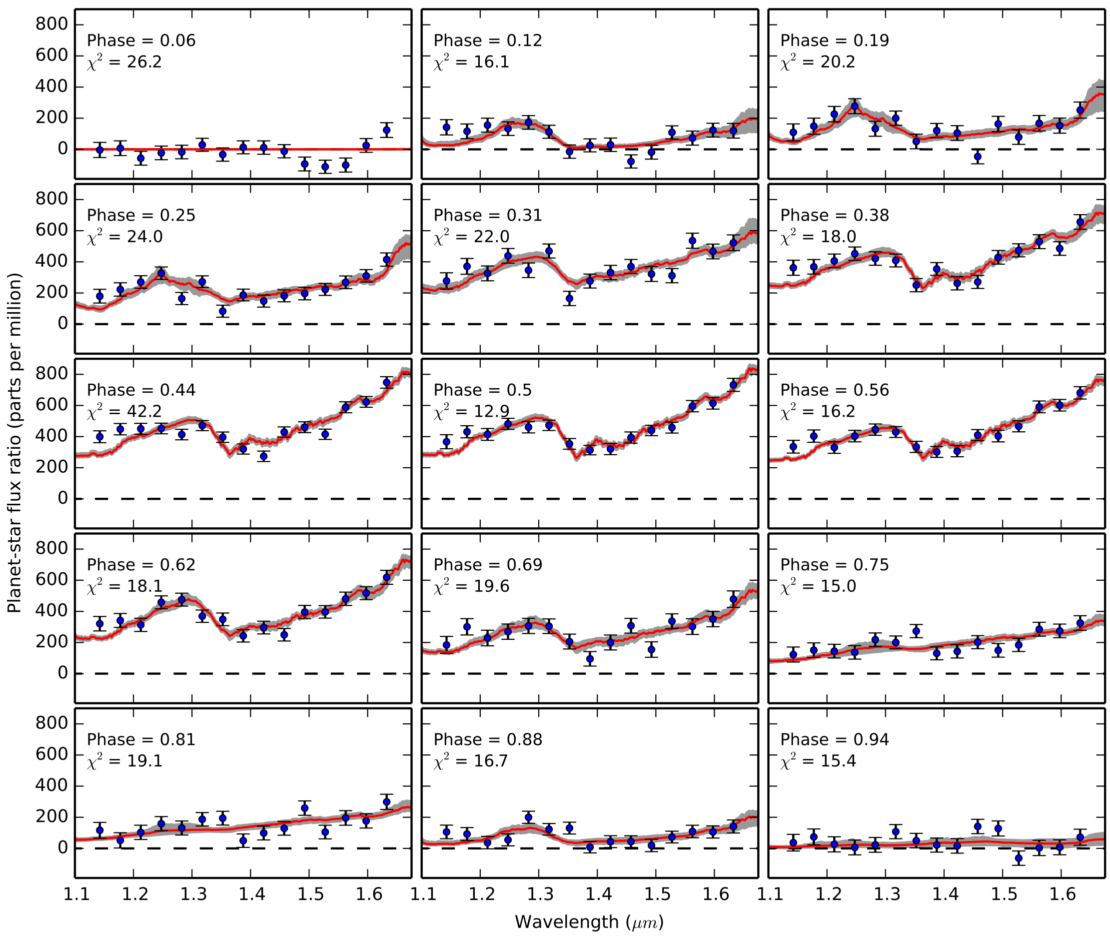

Fig. S 3: **Emission spectra of WASP-43b at fifteen binned orbital phases.** Although the data are subdivided into sixteen bins, the last bin occurs during transit (phase = 0.0), when we have no information about the planet's thermal emission. Red lines indicate median models to the blue data points with 1σ uncertainties. The gray regions indicate model 1σ uncertainty regions.

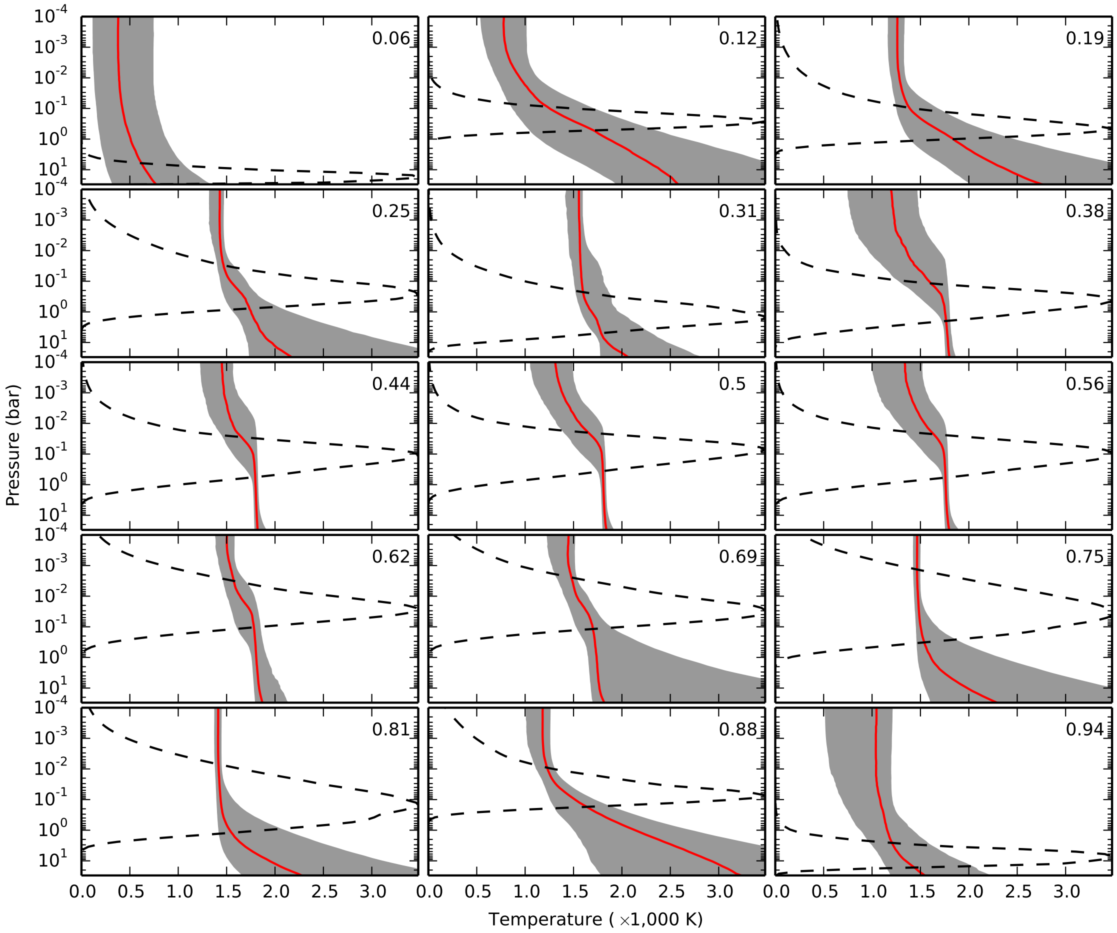

Fig. S 4: **Thermal profiles of WASP-43b at fifteen binned orbital phases.** Red curves depict median thermal profiles with gray 1σ uncertainty regions for the assumed parameterization of the retrieval. The dashed black curves are the WFC3 bandpass-averaged thermal emission contribution functions at each orbital phase. These contribution functions illustrate the atmospheric depths at which the observations probe. Therefore, the temperature retrieval results are most reliable within the pressure levels encompassed by the contribution functions. We infer temperatures outside of these regions based on the thermal profile parameterization and not by use of any priors.

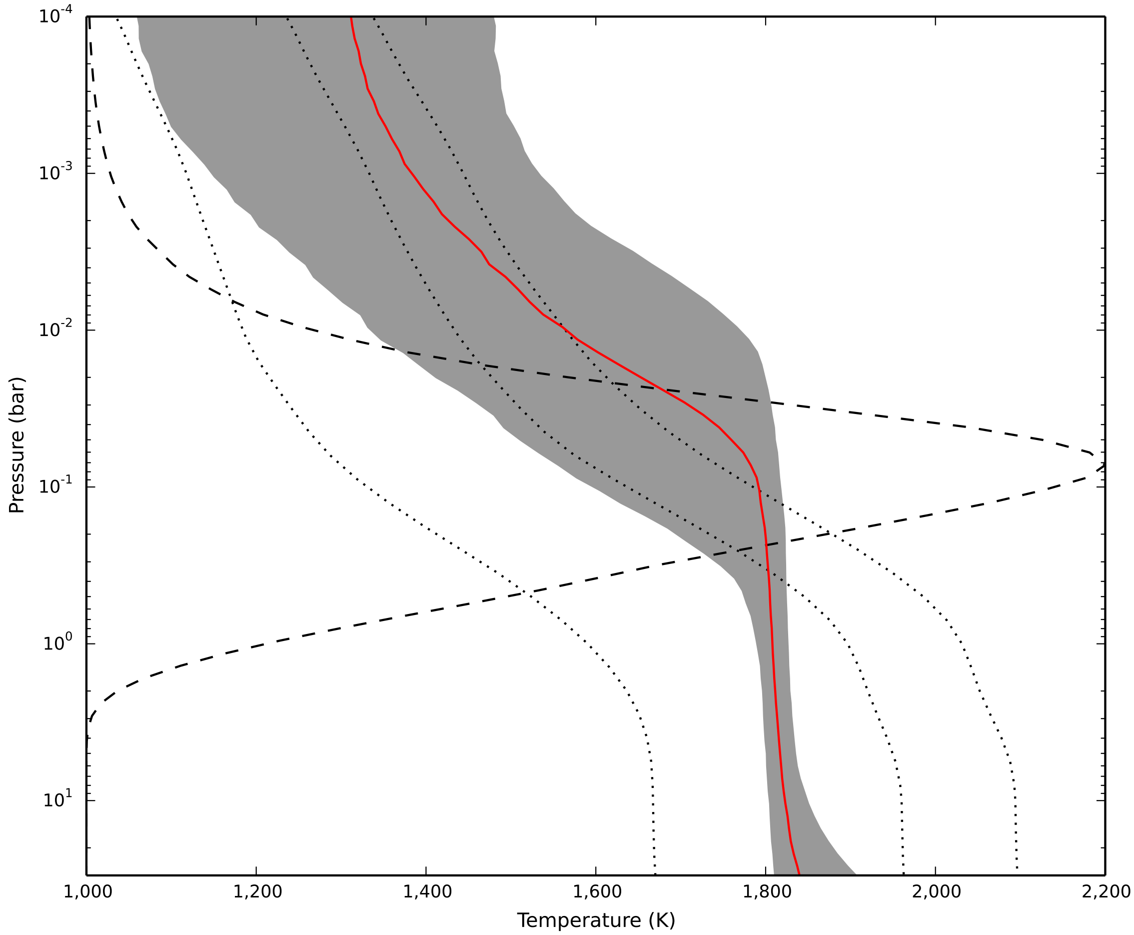

Fig. S 5: A comparison between the retrieved dayside and self-consistent temperature profiles. The solid red curve and gray region represent the median and 1σ uncertainty limits of the retrieved temperature profile from the WASP-43b secondary-eclipse data. The dashed black curve is the averaged thermal emission contribution function over the WFC3 bandpass. The dotted black curves are the temperature profiles computed from a self-consistent radiative equilibrium model (*27*). They represent, from cool to hot respectively, 4π (full planet) heat redistribution, 2π (dayside only) heat redistribution, and the substellar point. The retrieved thermal profile is consistent with the latter two radiative equilibrium models over the regions probed by these observations and best fits the self-consistent temperature profile at the substellar point. This suggests that the retrieval is heavily weighted towards fluxes from the substellar point and that the planet's day-night heat redistribution is inefficient, in accordance with the phase curve.

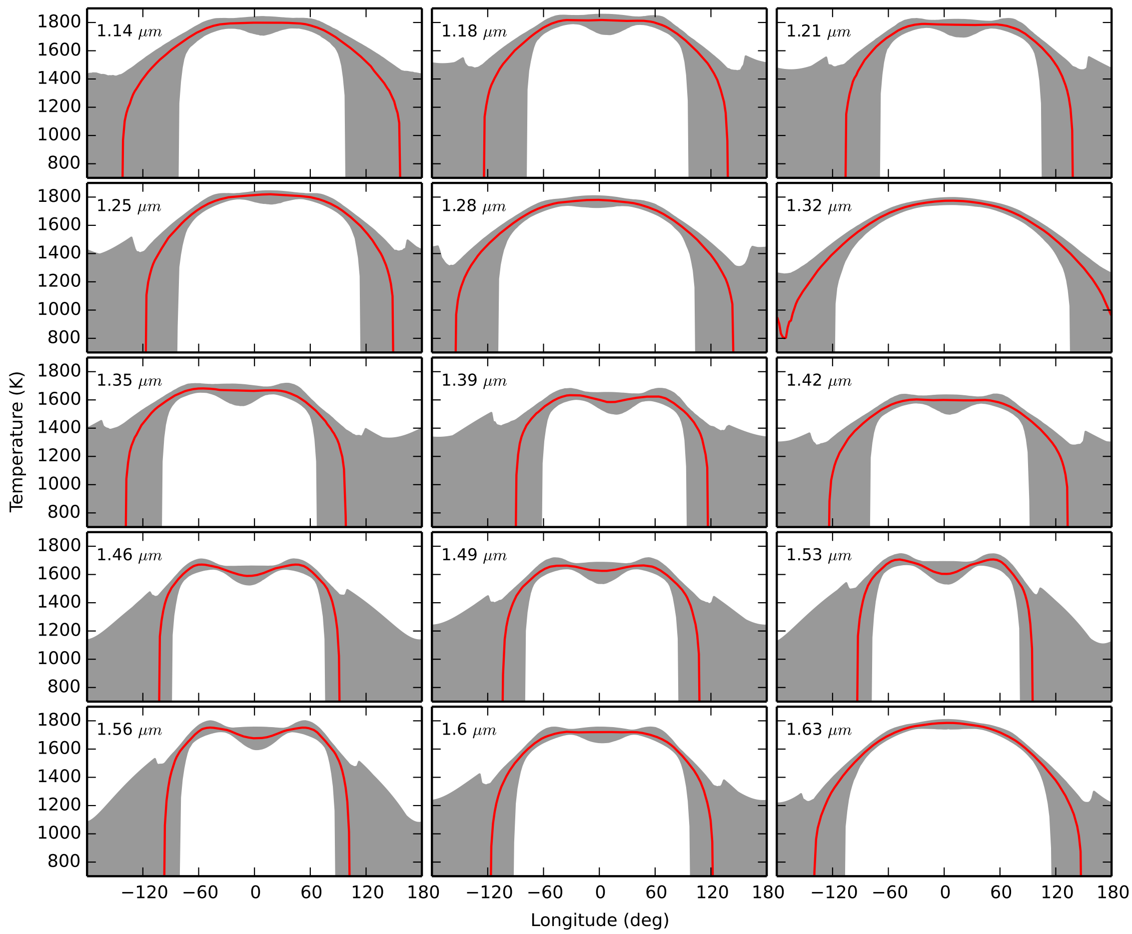

Fig. S 6: **Longitudinally-resolved brightness temperatures at fifteen spectrophotometric channels.** Red lines indicate median models and gray regions depict 1σ uncertainty regions. We generate these models by inverting 1,000 phase curves per spectroscopic channel from our DEMCMC analysis into longitudinally-dependent light curves by way off a least-squares minimizer, computing the brightness temperatures for each model at every longitude, and then estimating the asymmetric uncertainty regions about the median. Near the night side, all of the uncertainties extend down to 0 K, thus indicating no lower constraints on the night-side temperatures. The apparent dips in the median fits near the expected peak hotspots ($\sim 0°$) in some channels is a byproduct of our sinusoidal model parameterization. To account for the absence of measured flux on the planet's night-side within the water band and the strong dayside emission, we require a steep temperature gradient near the terminator. To prevent the sinusoidal model from over-predicting the dayside temperature, a second sinusoid dampens the model at the peak. Over-dampening of the peaks is what causes these apparent dips.

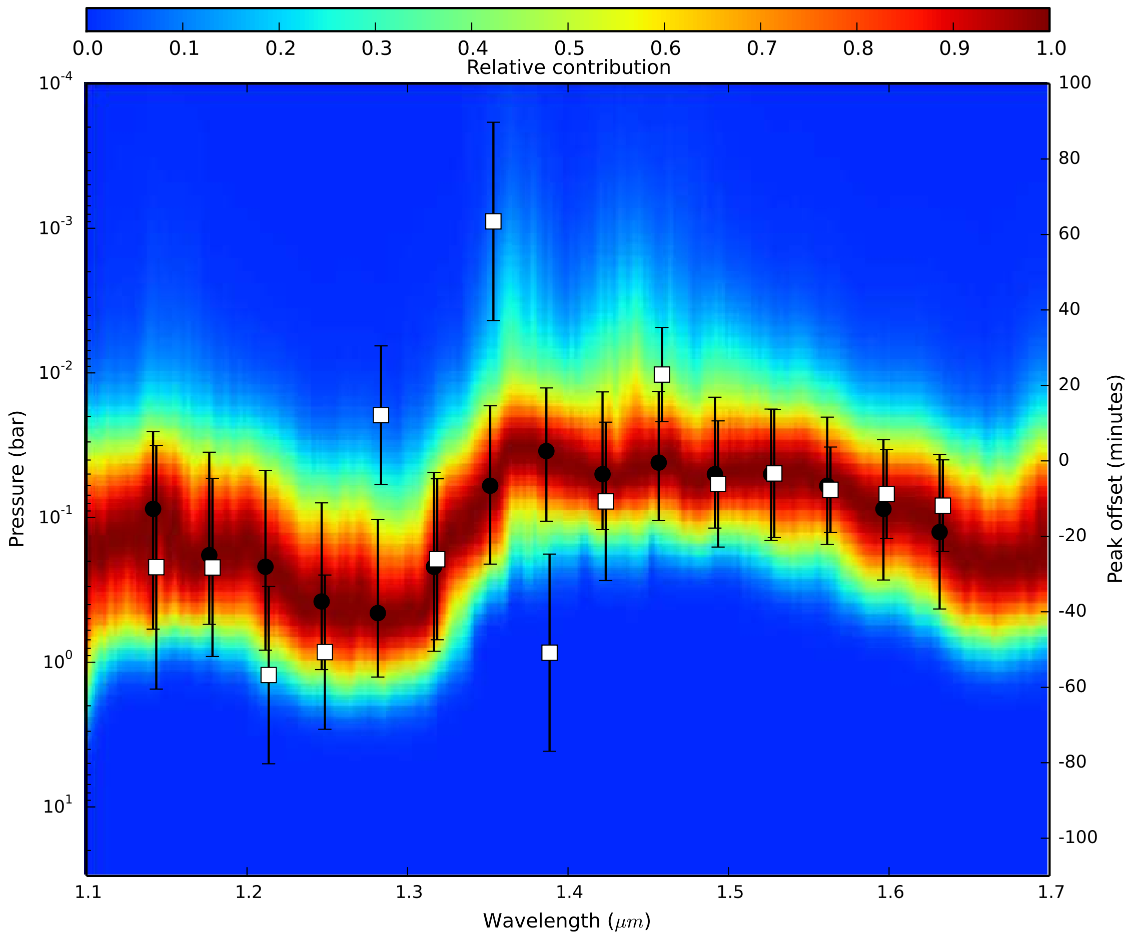

Fig. S 7: **Dayside thermal emission contribution function of WASP-43b.** The function is computed using the median values from the secondary-eclipse retrieval. Red indicates the pressure levels at which the optical depth is unity. These regions have the most significant contribution to the wavelength-dependent emission. Blue indicates regions with negligible contribution to the total emission. At high pressures, the column of gas is too dense for the slant rays to penetrate and, at low pressures, the column density is too low for the gas to significantly impact the spectrum. Black circles signify the pressure level at peak contribution in each spectrophotometric channel and vertical lines represent the full-width at half maximum. The dayside emission emanates primarily between 0.01 and 1 bar. White squares with 1σ uncertainties represent the phase-curve peak offsets from Table S2 (scaling on right axis). Despite the outliers, there is a visible correlation between the dayside thermal emission contribution levels and phase-curve peak offsets as a function of wavelength.

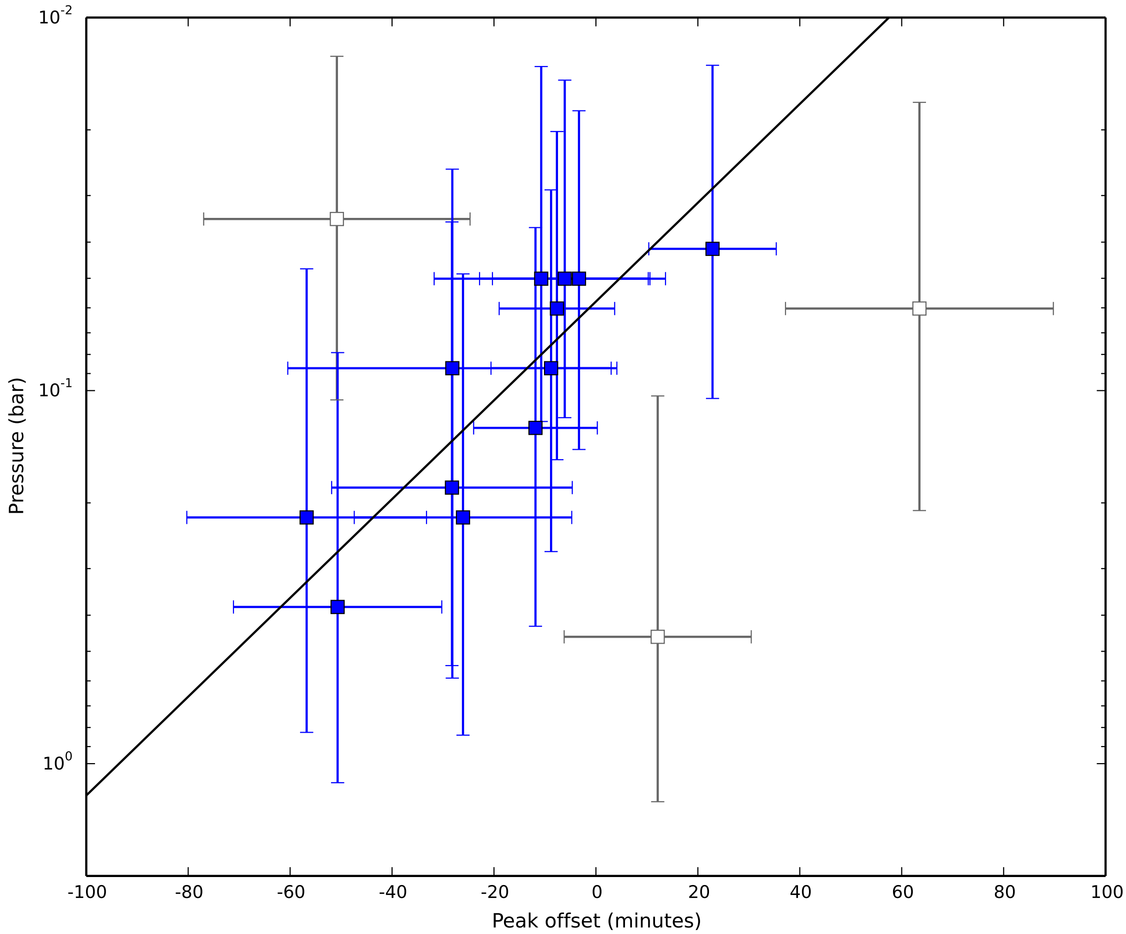

Fig. S 8: **Correlation between the dayside thermal emission contribution level and phase-curve peak offset.** The vertical error bars represent the full-width at half maxima from Fig. S7 and the horizontal error bars are 1σ peak offset uncertainties from Table S2. We use orthogonal distance regression to fit a linear model (black line) to the 12 good channels (blue squares) and measure a slope with a significance of 5.6σ with respect to the null hypothesis (no correlation). These data have a Pearson product-moment correlation coefficient of -0.85, where 0 is no correlation and -1 is total inverse correlation. We use Chauvenet's criterion on the measured peak offsets to identify the three white squares as outliers. This can be seen in Fig. S7 where the 1.2825, 1.3525, and 1.3875 μm channels do not have peak offsets that vary smoothly with wavelength as influenced by the broad water feature. At higher atmospheric pressures, we detect a stronger deviation in the phase-curve peak offset relative to the time of secondary eclipse. This trend qualitatively matches the predictions of three-dimensional circulation models.

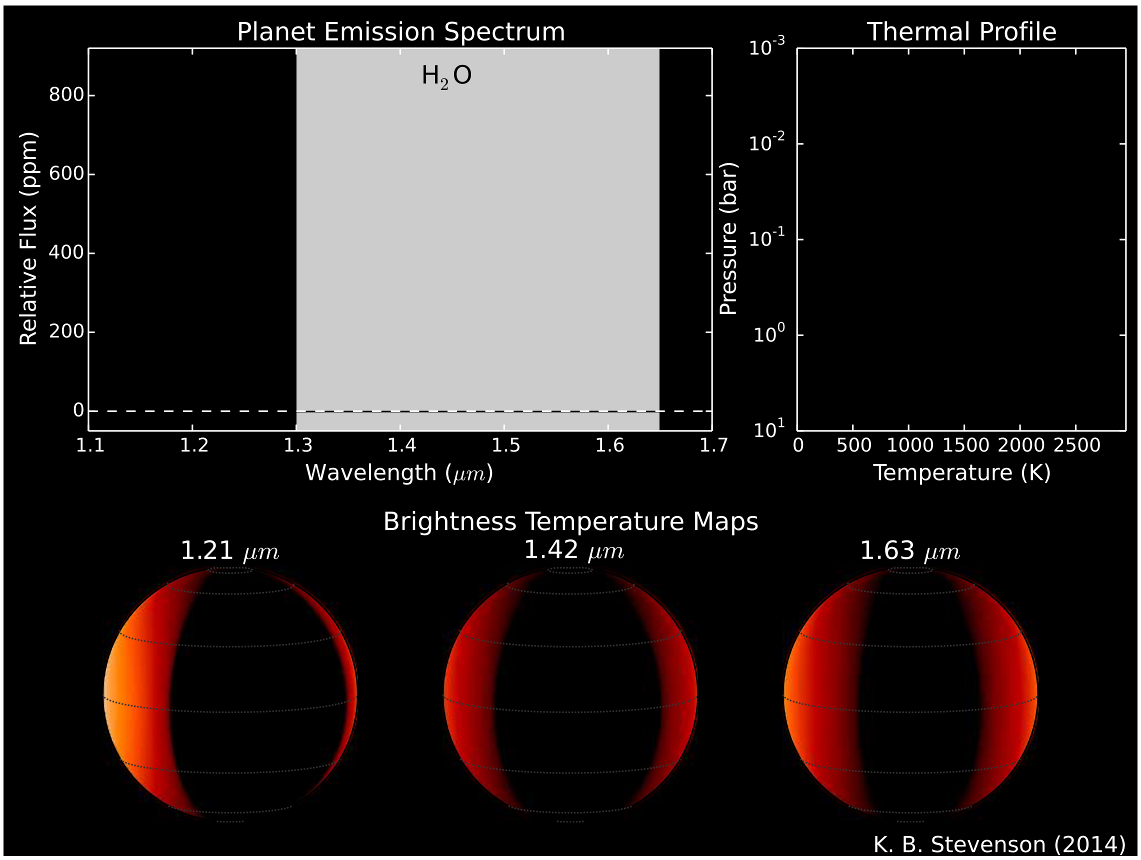

Movie S 1: Time-lapse video of WASP-43b over one planet rotation. The left and right panels display the phase-resolved emission spectrum and thermal profile, respectively, with 1σ uncertainty regions. There is a broad water absorption feature from 1.35 to 1.6 µm. The rotating spheres depict longitudinally-resolved brightness temperature maps in three spectrophotometric channels.

References

1. H. A. Knutson, D. Charbonneau, L. E. Allen, J. J. Fortney, E. Agol, N. B. Cowan, A. P. Showman, C. S. Cooper, S. T. Megeath, A map of the day-night contrast of the extrasolar planet HD 189733b. *Nature* **447**, 183–186 (2007). Medline doi:10.1038/nature05782

2. H. A. Knutson, D. Charbonneau, N. B. Cowan, J. J. Fortney, A. P. Showman, E. Agol, G. W. Henry, The 8 μm phase variation of the hot Saturn HD 149026b. *Astrophys. J.* **703**, 769–784 (2009). doi:10.1088/0004-637X/703/1/769

3. I. J. M. Crossfield, B. M. S. Hansen, J. Harrington, J. Y.-K. Cho, D. Deming, K. Menou, S. Seager, A new 24 μm phase curve for υ Andromedae b. *Astrophys. J.* **723**, 1436–1446 (2010). doi:10.1088/0004-637X/723/2/1436

4. N. B. Cowan, P. Machalek, B. Croll, L. M. Shekhtman, A. Burrows, D. Deming, T. Greene, J. L. Hora, Thermal phase variations of WASP-12b: Defying predictions. *Astrophys. J.* **747**, 82 (2012). doi:10.1088/0004-637X/747/1/82

5. H. A. Knutson, N. Lewis, J. J. Fortney, A. Burrows, A. P. Showman, N. B. Cowan, E. Agol, S. Aigrain, D. Charbonneau, D. Deming, J.-M. Désert, G. W. Henry, J. Langton, G. Laughlin, 3.6 AND 4.5 μm phase curves and evidence for non-equilibrium chemistry in the atmosphere of extrasolar planet HD 189733b. *Astrophys. J.* **754**, 22 (2012). doi:10.1088/0004-637X/754/1/22

6. N. K. Lewis, H. A. Knutson, A. P. Showman, N. B. Cowan, G. Laughlin, A. Burrows, D. Deming, J. R. Crepp, K. J. Mighell, E. Agol, G. Á. Bakos, D. Charbonneau, J.-M. Désert, D. A. Fischer, J. J. Fortney, J. D. Hartman, S. Hinkley, A. W. Howard, J. A. Johnson, M. Kao, J. Langton, G. W. Marcy, Orbital phase variations of the eccentric giant planet HAT-P-2b. *Astrophys. J.* **766**, 95 (2013). doi:10.1088/0004-637X/766/2/95

7. P. F. L. Maxted, D. R. Anderson, A. P. Doyle, M. Gillon, J. Harrington, N. Iro, E. Jehin, D. Lafreniere, B. Smalley, J. Southworth, Spitzer 3.6 and 4.5 m full-orbit light curves of WASP-18. *Mon. Not. R. Astron. Soc.* **428**, 2645–2660 (2013). doi:10.1093/mnras/sts231

8. S. Seager, D. D. Sasselov, Extrasolar giant planets under strong stellar irradiation. *Astrophys. J.* **502**, L157–L161 (1998). doi:10.1086/311498

9. A. Burrows, T. Guillot, W. B. Hubbard, M. S. Marley, D. Saumon, J. I. Lunine, D. Sudarsky, On the radii of close-in giant planets. *Astrophys. J.* **534**, L97–L100 (2000). Medline doi:10.1086/312638

10. T. Guillot, A. P. Showman, Evolution of "51 Pegasus b-like" planets. *Astron. Astrophys.* **385**, 156–165 (2002). doi:10.1051/0004-6361:20011624

11. D. Sudarsky, A. Burrows, I. Hubeny, Theoretical spectra and atmospheres of extrasolar giant planets. *Astrophys. J.* **588**, 1121–1148 (2003). doi:10.1086/374331

12. J. J. Fortney, C. S. Cooper, A. P. Showman, M. S. Marley, R. S. Freedman, The influence of atmospheric dynamics on the infrared spectra and light curves of hot Jupiters. *Astrophys. J.* **652**, 746–757 (2006). doi:10.1086/508442

13. C. Hellier, D. R. Anderson, A. Collier Cameron, M. Gillon, E. Jehin, M. Lendl, P. F. L. Maxted, F. Pepe, D. Pollacco, D. Queloz, D. Ségransan, B. Smalley, A. M. S. Smith, J. Southworth, A. H. M. J. Triaud, S. Udry, R. G. West, WASP-43b: The closest-orbiting hot Jupiter. *Astron. Astrophys.* **535**, L7 (2011). doi:10.1051/0004-6361/201117081

14. M. Gillon, A. H. M. J. Triaud, J. J. Fortney, B.-O. Demory, E. Jehin, M. Lendl, P. Magain, P. Kabath, D. Queloz, R. Alonso, D. R. Anderson, A. Collier Cameron, A. Fumel, L. Hebb, C. Hellier, A. Lanotte, P. F. L. Maxted, N. Mowlavi, B. Smalley, The TRAPPIST survey of southern transiting planets. *Astron. Astrophys.* **542**, A4 (2012). doi:10.1051/0004-6361/201218817

15. W. Wang, R. van Boekel, N. Madhusudhan, G. Chen, G. Zhao, T. Henning, Ground-based detections of thermal emission from the dense hot Jupiter WASP-43b in the *H* and K_s bands. *Astrophys. J.* **770**, 70 (2013). doi:10.1088/0004-637X/770/1/70

16. G. Chen, R. van Boekel, H. Wang, N. Nikolov, J. J. Fortney, U. Seemann, W. Wang, L. Mancini, T. Henning, Broad-band transmission spectrum and K-band thermal emission of WASP-43b as observed from the ground. *Astron. Astrophys.* **563**, A40 (2014). doi:10.1051/0004-6361/201322740

17. J. Blecic, J. Harrington, N. Madhusudhan, K. B. Stevenson, R. A. Hardy, P. E. Cubillos, M. Hardin, O. Bowman, S. Nymeyer, D. R. Anderson, C. Hellier, A. M. S. Smith, A. C. Cameron, *SPITZER* observations of the thermal emission from WASP-43b. *Astrophys. J.* **781**, 116 (2014). doi:10.1088/0004-637X/781/2/116

18. K. B. Stevenson, J. L. Bean, A. Seifahrt, J.-M. Désert, N. Madhusudhan, M. Bergmann, L. Kreidberg, D. Homeier, Transmission spectroscopy of the hot Jupiter WASP-12b from 0.7 TO 5 μm. *Astron. J.* **147**, 161 (2014). doi:10.1088/0004-6256/147/6/161

19. Materials and methods are available as supplementary material on *Science* Online .

20. K. Mandel, E. Agol, Analytic light curves for planetary transit searches. *Astrophys. J.* **580**, L171–L175 (2002). doi:10.1086/345520

21. L. Kreidberg, J. L. Bean, J. M. Désert, B. Benneke, D. Deming, K. B. Stevenson, S. Seager, Z. Berta-Thompson, A. Seifahrt, D. Homeier, Clouds in the atmosphere of the super-Earth exoplanet GJ 1214b. *Nature* **505**, 69–72 (2014). Medline doi:10.1038/nature12888

22. M. R. Line, H. Knutson, A. S. Wolf, Y. L. Yung, A systematic retrieval analysis of secondary eclipse spectra. II. A uniform analysis of nine planets and their C to O Ratios. *Astrophys. J.* **783**, 70 (2014). doi:10.1088/0004-637X/783/2/70

23. V. Parmentier, G. Guillot, *VizieR Online Data Catalog* **356**, 29133 (2013).

24. L. Kreidberg, J. L. Bean, J.-M. Désert, M. R. Line, J. J. Fortney, N. Madhusudhan, K. B. Stevenson, A. P. Showman, D. Charbonneau, P. R. McCullough, S. Seager, A.

Burrows, G. W. Henry, M. Williamson, T. Kataria, D. Homeier, A precise water abundance measurement for the hot Jupiter WASP-43b. *Astrophys. J.* **793**, L27 (2014). doi:10.1088/2041-8205/793/2/L27

25. D. Perez-Becker, A. P. Showman, Atmospheric heat redistribution on hot Jupiters. *Astrophys. J.* **776**, 134 (2013). doi:10.1088/0004-637X/776/2/134
26. M. S. Marley, C. Gelino, D. Stephens, J. I. Lunine, R. Freedman, Reflected spectra and albedos of extrasolar giant planets. I. Clear and cloudy atmospheres. *Astrophys. J.* **513**, 879–893 (1999). doi:10.1086/306881
27. A. Burrows, L. Ibgui, I. Hubeny, Optical albedo theory of strongly irradiated giant planets: The case of HD 209458b. *Astrophys. J.* **682**, 1277–1282 (2008). doi:10.1086/589824
28. J. J. Fortney, K. Lodders, M. S. Marley, R. S. Freedman, A unified theory for the atmospheres of the hot and very hot Jupiters: Two classes of irradiated atmospheres. *Astrophys. J.* **678**, 1419–1435 (2008). doi:10.1086/528370
29. N. B. Cowan, E. Agol, Inverting phase functions to map exoplanets. *Astrophys. J.* **678**, L129–L132 (2008). doi:10.1086/588553
30. A. P. Showman, T. Guillot, Atmospheric circulation and tides of "51 Pegasus b-like" planets. *Astron. Astrophys.* **385**, 166–180 (2002). doi:10.1051/0004-6361:20020101
31. C. S. Cooper, A. P. Showman, Dynamic meteorology at the photosphere of HD 209458b. *Astrophys. J.* **629**, L45–L48 (2005). doi:10.1086/444354
32. A. P. Showman, J. J. Fortney, Y. Lian, M. S. Marley, R. S. Freedman, H. A. Knutson, D. Charbonneau, Atmospheric circulation of hot Jupiters: Coupled radiative-dynamical general circulation model simulations of HD 189733b and HD 209458b. *Astrophys. J.* **699**, 564–584 (2009). doi:10.1088/0004-637X/699/1/564
33. E. Buenzli, D. Apai, C. V. Morley, D. Flateau, A. P. Showman, A. Burrows, M. S. Marley, N. K. Lewis, I. N. Reid, Vertical atmospheric structure in a variable brown dwarf: Pressure-dependent phase shifts in simultaneous *Hubble Space Telescope* - *Spitzer* light curves. *Astrophys. J.* **760**, L31 (2012). doi:10.1088/2041-8205/760/2/L31
34. A. Burrows, E. Rauscher, D. S. Spiegel, K. Menou, Photometric and spectral signatures of three-dimensional models of transiting giant exoplanets. *Astrophys. J.* **719**, 341–350 (2010). doi:10.1088/0004-637X/719/1/341